

# Probing the Li Insertion Mechanism of ZnFe<sub>2</sub>O<sub>4</sub> in Li-Ion Batteries: A Combined X-Ray Diffraction, Extended X-Ray Absorption Fine Structure, and Density Functional Theory Study

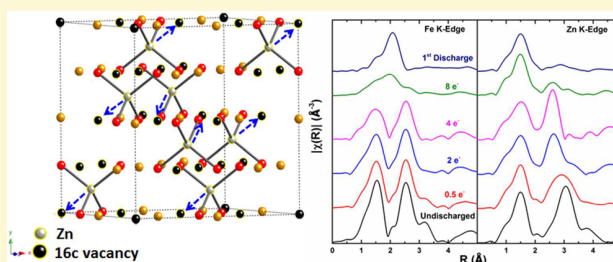
Yiman Zhang,<sup>†</sup> Christopher J. Pelliccione,<sup>§</sup> Alexander B. Brady,<sup>‡</sup> Haoyue Guo,<sup>†</sup> Paul F. Smith,<sup>†</sup> Ping Liu,<sup>§</sup> Amy C. Marschlok,<sup>\*,†,‡,§</sup> Kenneth J. Takeuchi,<sup>\*,†,‡</sup> and Esther S. Takeuchi<sup>\*,†,§,‡,§</sup>

<sup>†</sup>Department of Chemistry and <sup>‡</sup>Department of Materials Science and Engineering, Stony Brook University, Stony Brook, New York 11790, United States

<sup>§</sup>Energy Sciences Directorate, Brookhaven National Laboratory, Upton, New York 11973, United States

## Supporting Information

**ABSTRACT:** We report an extensive study on fundamental properties that determine the functional electrochemistry of ZnFe<sub>2</sub>O<sub>4</sub> spinel (theoretical capacity of 1000 mAh/g). For the first time, the reduction mechanism is followed through a combination of in situ X-ray diffraction data, synchrotron based powder diffraction, and ex-situ extended X-ray absorption fine structure allowing complete visualization of reduction products irrespective of their crystallinity. The first 0.5 electron equivalents (ee) do not significantly change the starting crystal structure. Subsequent lithiation results in migration of Zn<sup>2+</sup> ions from 8a tetrahedral sites into vacant 16c sites. Density functional theory shows that Li<sup>+</sup> ions insert into 16c site initially and then 8a site with further lithiation. Fe metal is formed over the next eight ee of reduction with no evidence of concurrent Zn<sup>2+</sup> reduction to Zn metal. Despite the expected formation of LiZn alloy from the electron count, we find no evidence for this phase under the tested conditions. Additionally, upon oxidation to 3 V, we observe an FeO phase with no evidence of Fe<sub>2</sub>O<sub>3</sub>. Electrochemistry data show higher electron equivalent transfer than can be accounted for solely based on ZnFe<sub>2</sub>O<sub>4</sub> reduction indicating excess capacity ascribed to carbon reduction or surface electrolyte interphase formation.



## INTRODUCTION

Zinc ferrite (ZnFe<sub>2</sub>O<sub>4</sub>, ZFO) was first reported as a lithium ion battery anode in 2004.<sup>1</sup> It is an ordered spinel in which the O<sup>2-</sup> ions form a cubic close packed structure, in which Zn<sup>2+</sup> preferentially occupies tetrahedral sites (8a) and Fe<sup>3+</sup> preferentially occupies octahedral sites (16d). This structure also includes vacant sites (16c) (Figure 1). There are two 16c vacant sites per formula unit (ZnFe<sub>2</sub>O<sub>4</sub>).

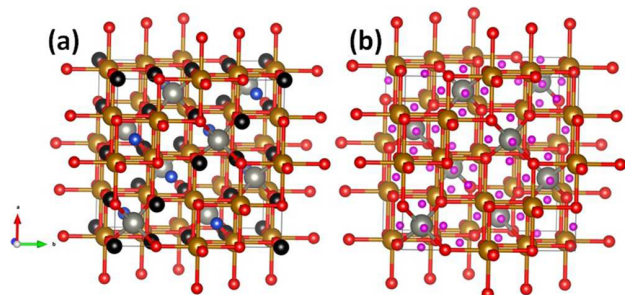
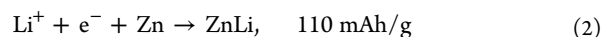
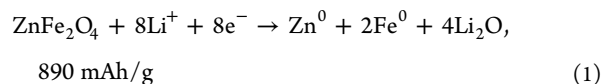
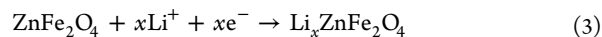


**Figure 1.** Unit cell of ZnFe<sub>2</sub>O<sub>4</sub> (gray, Zn; red, O; brown, Fe) showing the 16c (black) and 8b (blue) vacant sites in panel a and 48f (pink) vacant sites in panel b.

One intriguing aspect of this spinel structure is that a high theoretical capacity of 1000 mAh/g can be predicted in Li based batteries assuming full conversion of Fe<sup>3+</sup> to Fe<sup>0</sup> and Zn<sup>2+</sup> to Zn<sup>0</sup> followed by formation of a Zn–Li alloy, eqs 1 and 2:



The reduction mechanism is widely believed to proceed first via formation of a lithium intercalated spinel in which Li<sup>+</sup> ions insert into the vacant 16c sites, eq 3:

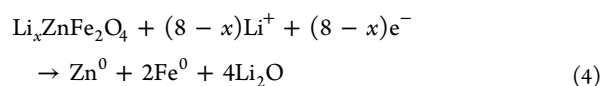


In general, *x* is reported within the range of 0.2–2, depending on the first discharge plateau.<sup>2,3</sup> For *x* > 2, the remainder of the discharge proceeds through as yet unidentified intermediates to form metallic species:

Received: February 4, 2017

Revised: April 24, 2017

Published: April 24, 2017



ZnFe<sub>2</sub>O<sub>4</sub> shape, morphology, and the presence of carbon additives can all affect the above reduction process. ZFO hollow spheres,<sup>4</sup> nanofibers,<sup>5</sup> and nano-octahedrons<sup>6</sup> have been explored in lithiation process, which demonstrate an average of 900 mAh/g capacity retained after 30 cycles at 60 mA/g discharge current density. With carbon additives, including multiwall carbon nanotubes,<sup>7</sup> graphene,<sup>8</sup> and amorphous carbon,<sup>9–11</sup> the electrodes have achieved over 1000 mAh/g theoretical capacity for the initial discharge at a C/50 rate and maintained a high capacity of 1000 mAh/g until 100 cycles with a 40 mA/g discharged current density. The ZFO reduction profile has a characteristic long electrochemical plateau at around 0.7 V, where carbon reduction or solid electrolyte interface (SEI) layer can occur simultaneously. SEI components in the carbon coated ZFO electrodes were assigned based on Raman data as poly(ethylene oxide) and alkyl carbonate species. Also, the formation of AsF<sub>N</sub> complex within the 40 nm SEI layer thickness when using LiAsF<sub>6</sub> as the electrolyte salt, measured with As K-edge absorption spectroscopies, provides further evidence.<sup>12,13</sup> Previous studies have utilized techniques that monitor crystalline phase transformations (e.g., X-ray diffraction, XRD) on either Zn ferrite<sup>9</sup> or iron metal oxides.<sup>14,15</sup> These techniques, however, do not detect amorphous or nanocrystalline phases, which most commonly form at the end of discharge for metal oxide electrodes.<sup>16</sup>

Prior literature reports propose that the LiZn alloy is expected to form and would account for one electron equivalent when observed from discharge current. However, experimental identification of LiZn formed from reduced ZFO to our knowledge exists in only two reports,<sup>1,4</sup> where the most compelling evidence for its presence is the LiZn alloy (111) diffraction peak identified by PXRD and selected area electron diffraction (SAED)/transmission electron microscopy (TEM) in the ex-situ electrodes reduced down to below 0.01 V. When considering that one study on ZnO anodes found only a small fraction of reduced Zn nanoparticles further reduce to LiZn by extended X-ray absorption fine structure (EXAFS),<sup>17</sup> a key focus of this study is to identify whether alloy formation can be observed under more typical discharge conditions and whether it can account for the delivered capacity.

The oxidation process is widely assumed to form ZnO and Fe<sub>2</sub>O<sub>3</sub>.<sup>6,18–23</sup> This assumption is partly based on ZFO's capability to retain high capacity (~90% theoretical, frequently in excess of 50 cycles). However, to our knowledge, definitive structural identification of these oxidation products is mostly used by ex situ SAED/TEM technique. Of these, the first such study assigned FeO, not Fe<sub>2</sub>O<sub>3</sub>, as the oxidation product.<sup>2</sup> Subsequent reports, which assigned Fe<sub>2</sub>O<sub>3</sub>,<sup>4,6,24</sup> have done so while citing Mössbauer studies, which find Fe<sup>3+</sup> in electrochemically oxidized NiFe<sub>2</sub>O<sub>4</sub> or CoFe<sub>2</sub>O<sub>4</sub>.<sup>25,26</sup> However, we note that Mössbauer has also identified Fe<sup>3+</sup> from reduced FeO electrodes,<sup>27</sup> which may also be assigned to a 3FeO = Fe<sup>0</sup> + Fe<sub>2</sub>O<sub>3</sub> disproportionation reaction.<sup>28,29</sup> Hence, understanding the formation of FeO or Fe<sub>2</sub>O<sub>3</sub> during oxidation is a key focus of this study to determine the recharge electron counts from ZFO electrode. Our group has recently studied the reduction and oxidation mechanisms of a close structural analog, magnetite (Fe<sub>3</sub>O<sub>4</sub>), by scanning transmission electron microscopy (STEM)-electron energy loss spectroscopy (EELS) and

X-ray absorption spectroscopy (XAS) techniques.<sup>30</sup> We found no evidence of Fe<sup>3+</sup> in electrochemically oxidized electrodes, suggesting the presence of a second metal (Zn, Ni, Co) may allow Fe to access higher oxidation states on oxidation. Such a finding is critical to advance the design of materials which can retain high capacities with cycling.

Herein, ZnFe<sub>2</sub>O<sub>4</sub> nanoparticles were synthesized via precipitation followed by a hydrothermal treatment. The electrochemical testing of as synthesized material is conducted in lithium-based batteries. The structural evolution and species identification of the ZFO electrode as a function of discharge and charge are reported here by means of in situ XRD, and ex situ extended X-ray absorption spectroscopy of both Fe and Zn K-edge. X-ray powder diffraction (XPD) from a synchrotron source is applied to determine the site occupancy of the LiZnFe<sub>2</sub>O<sub>4</sub> phase, and Pair distribution function (PDF) is used to identify the amorphous species at the fully discharged state. Further, density functional theory (DFT) calculations were carried out to gain better understanding of the intermediate structures and mechanism for the initial reduction process.

## EXPERIMENTAL METHODS

**Synthesis and Characterization.** *Synthesis.* All chemicals used in the experiment were of analytical grade and used as received. ZnFe<sub>2</sub>O<sub>4</sub> (ZFO) nanomaterials were prepared using a precipitation method followed by hydrothermal reaction using DI water as solvent. Briefly, stoichiometric solutions of Zn and Fe are added concurrently to a DI water solution of excess triethylamine in an ice bath. The precipitate is collected, vacuum-dried, then treated hydrothermally at 220 °C for 12 h. The final sample is vacuum-dried.

*Materials Characterization.* XRD measurements were collected using a Rigaku Smartlab diffractometer with Cu K $\alpha$  radiation for initial phase determination. Quantitative elemental analysis of zinc and iron was determined by inductively coupled plasma-optical emission spectroscopy (ICP-OES) performed using a ThermoScientific iCap 6000 ICP spectrometer. TEM images of Zn ferrite were obtained using a JEOL JEM 1400 instrument. N<sub>2</sub> sorption (adsorption–desorption) measurements were performed with a Quantachrome Nova 4200e instrument and a multipoint BET (Brunauer, Emmett, and Teller) method was used for calculating the surface area.

*Electrochemical Methods.* Some electrodes were prepared using a slurry cast method with ZFO as active material combined with carbon and polyvinylidene fluoride binder at a mass composition of 70:20:10. Additional pellet electrodes were prepared using either 100% ZnFe<sub>2</sub>O<sub>4</sub> or a mixture of 90% ZFO and 10% carbon and were used as electrodes for full discharge and 1 ee reduction at C/50 rate (based on theoretical full discharge of 9 ee) discharge, respectively. Electrochemical cells were assembled using lithium metal as the counter electrode and 1 M LiPF<sub>6</sub> in ethylene carbonate and dimethyl carbonate at volume ratio of 30:70 electrolyte. The reduced ZFO material was recovered, sealed in polyimide tube in Ar-filled glovebox, and stored in inert atmosphere during the synchrotron X-ray powder diffraction measurement.

Cyclic voltammetry (CV) was applied to two electrode cells using lithium as the reference and counter electrode between 0.2 and 3.0 V at a scan rate of 0.1 mV/s for two cycles. The electrochemical cells were also tested in galvanostatic mode using voltage limits of 0.2 V for reduction and 3.0 V for oxidation. Cells were reduced using 100 mA/g (C/10) for the initial discharge mechanism study, electrodes were discharged to 0.5ee, 2ee, 4ee, 8ee, fully reduced (12ee), and then oxidized at 100 mA/g (C/10) rate to 3.0 V. All electrodes were recovered in glovebox and were sealed between polyimide tape for X-ray absorption spectroscopy measurements.

X-ray absorption spectroscopy (XAS) measurements of undischarged material, material reduced to 0.5ee, 2ee, 4ee, 8ee, fully reduced (12ee), and oxidized ZnFe<sub>2</sub>O<sub>4</sub> coatings were collected at the Materials Research Collaborative Access Team (MRCAT) beamline, Sector 10-BM, of the Advanced Photon Source at Argonne National Laboratory.

With a double crystal Si (111) monochromator, each sample was measured in transmission mode at both the Fe K-edge (7.112 keV) and Zn K-edge (9.659 keV) utilizing 22 cm long ionization chambers with 50:50 volume ratio of N<sub>2</sub>/He in the incident ion chamber and 85/15 N<sub>2</sub>/Ar in the transmission ion chamber. A Fe or Zn foil was used for initial beam energy calibration for each K-edge energy and was measured simultaneously with each experimental sample to ensure proper energy alignment of multiple scans.

The XAS spectra were aligned, merged, deglitched, and normalized using Athena.<sup>31</sup> The built-in AUTOBK algorithm was used to limit background contributions below  $R_{\text{bkg}} = 1.0 \text{ \AA}$ . Each spectrum was fit using  $k$ ,  $k^2$ , and  $k^3$   $k$ -weighting simultaneously with a  $k$ -range of 2.0–12.0  $\text{\AA}^{-1}$  and a Hanning window with  $dk = 2$ . The fitted  $R$ -range was typically 1.0–3.8  $\text{\AA}$  but was contracted to 1.0–3.1  $\text{\AA}$  in highly discharged samples. The  $R$ -range was selected to fully encompass the second shell peaks in the spectrum. Theoretical structural models based on ZnFe<sub>2</sub>O<sub>4</sub>,<sup>32</sup> FeO,<sup>33</sup> and Fe metal<sup>34</sup> crystal structures were created using FEFF6.<sup>35,36</sup> The selection of structural models used for each fit was dictated by the results of the fitted parameters: if the variables resulted in physically or statistically unreasonable values, the corresponding phase was removed from the overall model. In addition, to accurately track the relative amplitudes of each phase (and correspondingly the number of neighboring atoms), the  $S_0^2$  parameter, which accounts for intrinsic losses in the electron propagation and scattering process that governs XAS, was fit to either a Fe or Zn standard and was applied to all experimental fits.

Powder diffraction was performed at beamline 28-ID-1 (XPD-1) at the National Synchrotron Light Source-II (NSLS-II) at Brookhaven National Laboratory. Undischarged, 1ee, and fully discharged samples were sealed within a polyimide capillary with minimal exposure to atmosphere during data acquisition. The X-ray wavelength was calibrated to 0.18321  $\text{\AA}$ . Diffraction measurements were collected using a 16-in. CsI scintillator. The two-dimensional data were integrated to simulate a one-dimensional pattern using Fit2D software.<sup>37</sup> Rietveld refinement was conducted on the undischarged ZnFe<sub>2</sub>O<sub>4</sub> and 1ee electrochemically lithiated material utilizing GSAS-II to accurately obtain the lattice parameters, Debye-Wahler, site occupancy, and crystallite size.<sup>38</sup>

In addition to XRD measurements, atomic pair distribution function (PDF) measurements were also acquired at the XPD-1 beamline at NSLS-II on undischarged and fully discharged ZnFe<sub>2</sub>O<sub>4</sub> pellets. Conversion to PDF,  $G(r)$ , was performed using PDFGetX3 via a Fourier transform of the entire diffraction pattern.<sup>39</sup> A spectrum of an empty polyimide capillary was utilized for background removal before the conversion with  $Q_{\text{Max}}$  set to 20  $\text{\AA}^{-1}$  for both sample patterns.  $Q_{\text{Broad}}$  and  $Q_{\text{Damp}}$  were determined to be 0.0267 and 0.0188  $\text{\AA}^{-1}$ , respectively, by modeling a Ni standard and were applied to both experimental fits to accurately account for instrument related effects. The PDF patterns were analyzed using PDFgui<sup>40</sup> software in a  $R$ -range of 1–70  $\text{\AA}$ . A combination of ZnFe<sub>2</sub>O<sub>4</sub> and bcc Fe metal crystal structures were used to model the experimental data.

To evaluate the overall structure evolution during discharge of ZFO electrode, in situ X-ray diffraction was collected on Rigaku Miniflex during reduction and oxidation of ZnFe<sub>2</sub>O<sub>4</sub> electrode pouch cells controlled by a Biologic potentiostat using a C/10 rate. Each XRD scan took 33 min and corresponded to 0.5 electron equivalent transfer. The in situ cells delivered somewhat lower capacity than that observed in coin cells due to higher resistance of the pouch cell configuration compared to coin cell. However, the voltage plateau remains comparable and provides information regarding the structure change during reduction and oxidation.

**DFT Calculations.** DFT implemented in the Vienna ab initio simulation package (VASP) was employed.<sup>41,42</sup> The spin-polarized calculations were carried out with the PAW potential.<sup>43</sup> By using the PBE exchange-correlation functional<sup>44</sup> and a kinetic energy cut off of 520 eV, a Hubbard  $U$  correction of  $U_{\text{eff}} = 5.3 \text{ eV}$  was applied to the Fe  $d$  orbitals.<sup>30</sup> The tetrahedron smearing method with Blöchl corrections was used with the total energies converged better than  $10^{-4} \text{ eV}$ . The first Brillouin zone was sampled using a  $4 \times 4 \times 4$   $k$ -mesh. The nonlithiated and lithiated ZnFe<sub>2</sub>O<sub>4</sub> crystal structures were modeled

using Fd $\bar{3}m$  primitive cell, which included eight formula units. For ZnFe<sub>2</sub>O<sub>4</sub>, the DFT-optimized lattice parameters (8.54  $\text{\AA}$ ) and magnetic moments (4.3  $\mu\text{B}$ ) are in good agreement with the values measured experimentally (8.45  $\text{\AA}$  in Table 1; 4.2  $\mu\text{B}$ ).<sup>45</sup> To determine

**Table 1. Comparison of Fitting Results for As Synthesized and 1 ee Discharged ZFO;**

variable/sample	undischarged	1ee discharged
$R_{\text{wp}}$ of fit (%)	3.224 <sup>a</sup>	9.875
lattice parameter ( $a$ )	8.4508(1)	8.4977(5)
crystallite size (nm)	14.1(1)	14.0 (1)
microstrain (%)	0.450(2)	1.28(1)
Zn in 8a (% of the total Zn)	100	54.1(3)
Zn in 16c (% of total Zn)	0	45.8(4)
Fe in 16d (%)	100	100
Debye-Wahler: Zn	0.0068(1)	0.0040(5)
Debye-Wahler: Fe	0.0028(2)	0.0044(9)
Debye-Wahler: O	0.0058(5)	0.014(2)

<sup>a</sup>Graphic fitting is shown in Figure S3.

the position for each Li atom inserted into ZnFe<sub>2</sub>O<sub>4</sub>, a variety of possible vacancy sites were considered, where only the most stable configuration was chosen in our DFT calculations.

## RESULTS AND DISCUSSION

**Material Characterization Results.** ZFO was identified by powder X-ray diffraction, and Figure 2 shows the pattern along with the reference of PDF No. 01–089–7556. The position of the Bragg diffractions and their relative intensities match very well with the cubic spinel, space group Fd $\bar{3}m$ . The crystallite size was determined to be 11 nm based on the Scherrer equation<sup>46,47</sup> from the most intense (311) peak, which is consistent with the TEM images in Figure 3. Elemental analysis from ICP-OES showed a Zn/Fe ratio of 0.98:2, consistent with the expected stoichiometry. The specific surface area is 72 m<sup>2</sup>/g based on BET measurement with pore size of 6.5 nm (Figure 2b). The specific surface area is higher when compared to prior reports of ZFO nanorods (40.51 m<sup>2</sup>/g),<sup>48</sup> and ZFO nanofibers (11.6 m<sup>2</sup>/g),<sup>49</sup> which is due to the smaller size with different morphology. Previous reports have described specific surface areas as high as 112 m<sup>2</sup>/g for 10 nm ZFO nanoparticles, which is probably due to the larger pore size of the material (7.6 nm).<sup>50</sup>

**Electrochemical Testing and in Situ XRD.** Cyclic voltammetry was collected at a 0.1 mV/s sweep rate with voltage limits of 0.2 and 3.0 V for reduction and oxidation, respectively. The first cycle curve is shown in Figure 4a (black). Two small cathodic peaks can be observed at ~1.46 V (peak a) and ~1.04 V (peak b), followed by a major sharp peak at ~0.73 V (peak c). These peaks correspond to three observed plateaus in a galvanostatic reduction test, identified as peaks 1, 2, and 3 in Figure 4b. The first and last peaks also agree well with the DFT calculations (see below), which have values of 1.64, 1.58, and 0.89 V, respectively. Integration of total charge during each plateau yielded molar electron equivalents of 0.5 and 2 for peaks 1 and 2, respectively.

The total cycle 1 delivered capacity (1460 mAh/g, 13 electron equivalents) is larger than the theoretical capacity (1000 mAh/g, 111 mAh/g = 1 Li), likely due to contributions from SEI layer formation and carbon reduction in plateau 3.<sup>12,51</sup> The discharged electron equivalents assignment will be discussed below after the EXAFS analysis. To verify

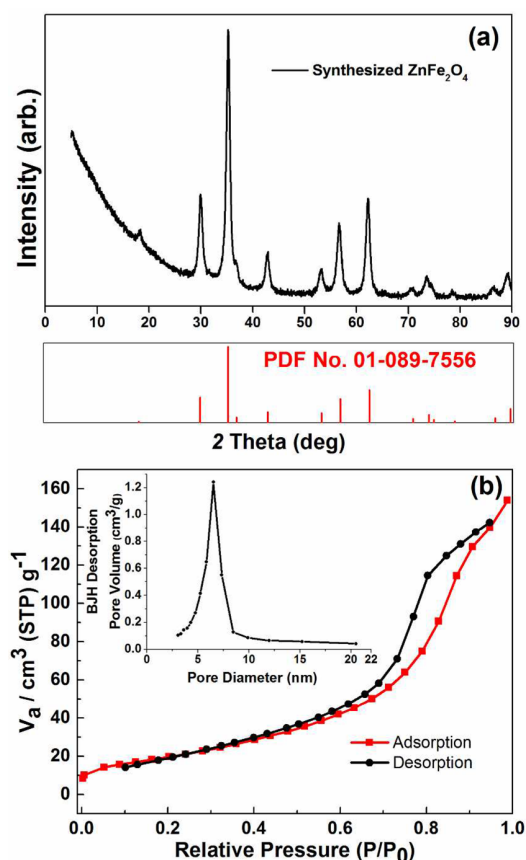


Figure 2. (a) X-ray powder diffraction of synthesized  $\text{ZnFe}_2\text{O}_4$  from Cu  $K\alpha$  wavelength and (b)  $\text{N}_2$  adsorption and desorption isotherms of  $\text{ZnFe}_2\text{O}_4$  nanoparticles. The inset in panel b is pore-size distribution.

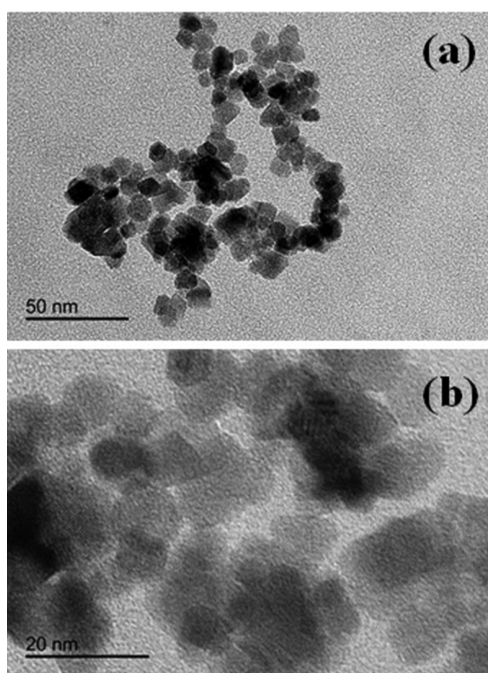


Figure 3. TEM images of  $\text{ZnFe}_2\text{O}_4$  material at different magnification: (a) 100k and (b) 300k.

the contributions from the carbon reduction, the background capacity of discharge from carbon alone cell (90% carbon with 10% binder) is determined, which gives the initial discharged capacity of 940.3 mAh/g (Figure S1), suggesting that 209 mAh/g capacity (around 2 ee) is due to carbon in the Zn ferrite electrode cell. On the first anodic potential sweep, there is one broad anodic peak centered at  $\sim 1.56$  V, which is consistent with the oxidation profile seen in the galvanostatic test, where one plateau with an operating voltage of 1.56 V is observed. These results indicate a first reduction occurring with insertion and conversion (phase change) mechanisms, followed by one phase change process on oxidation.

In the second cycle, the CV scan showed cathodic peaks at 1.23 V (d) and 0.92 V (e) (Figure 4a) and anodic peak at 1.6 V, which are shifted  $\sim 0.04$  V to higher potential compared with the cycle 1 anodic peak. The ZFO electrode demonstrated 880 mAh/g capacity (8ee) on cycle 2 during reduction with one plateau at an operating potential of 1.0 V, and 800 mAh/g capacity on oxidation with an operating potential at 1.75 V. These results indicate that subsequent reductions result in fewer phase changes than that in the first reduction.

To analyze the initial reduction in more detail, we first consider the prior literature suggesting that ZFO lithiates to  $\text{Li}_{0.5}\text{ZnFe}_2\text{O}_4$  and  $\text{Li}_2\text{ZnFe}_2\text{O}_4$  during the insertion process.<sup>4,7,19</sup> Because this first step is expected to yield crystalline products, we performed in situ XRD analysis. Figure 4c shows in situ XRD data taken at each 0.5 electron equivalent over the first 7.5 electron equivalents. The interferences from Cu and Li foil are indicated.

The ZFO (044) peak (62.02 deg) is chosen to identify the phase change during lithium insertion process. During discharge, the (044) peak shifted to a lower two theta angle from scan 1 to 3 and with a more dramatic change notable between scan 3 to scan 4 (Figure 4d), which is between 1.0 and 1.5 electron equivalents discharge.

To investigate the structure on the 1ee reduced sample in more detail, we performed synchrotron-level diffraction of the electrochemically obtained  $\text{LiZnFe}_2\text{O}_4$  material, Figure 5.

The graphical result of the Rietveld analysis of the synchrotron XPD data from the 1ee discharged material is shown in Figure 5 and the voltage profiles of 1ee and 0.2 V reduced electrode are shown in Figure S2. The  $\text{Fd}\bar{3}m$  crystal structure<sup>32</sup> and isotropic crystallite size and microstrain models were utilized for both refinements. Values for some important parameters are shown in Table 1.

Rietveld analysis of the lithiated (reduced) material ( $\text{LiZnFe}_2\text{O}_4$ ) shows that the lattice parameter has expanded (to  $8.4977 \pm 0.0005$  Å), which corresponds to a 0.56% expansion with respect to the starting lattice parameter of  $a = 8.4508 \pm 0.0001$  Å. This is notably less than that predicted by DFT (below) at only 0.56%, as opposed to 4.4%. Compared with the lithiation process of  $\text{CoFe}_2\text{O}_4$  spinel material,<sup>52</sup> which demonstrated a 2% lattice expansion at 0.55  $\text{Li}^+$  insertion per formula unit, the much smaller expansion at 1ee in our case may be due to the inherent 6.5 nm pore size of the synthesized  $\text{ZnFe}_2\text{O}_4$  material (Figure 2b).

The XPD refinement on  $\text{LiZnFe}_2\text{O}_4$  material reveals that 46% of the Zn has migrated to the 16c site, while 54% of the Zn remains in the 8a site at 1ee lithiation. This agrees almost perfectly with the DFT results, which predict a 50:50 split. Cation migrations during lithiation were also observed in other different cation spinel materials. Permien studied the lithiation process of  $(\text{Mn}_{0.7}\text{Fe}_{0.3})_{\text{A}}[\text{Mn}_{0.3}\text{Fe}_{1.7}]_{\text{B}}\text{O}_4$  material using<sup>57</sup>

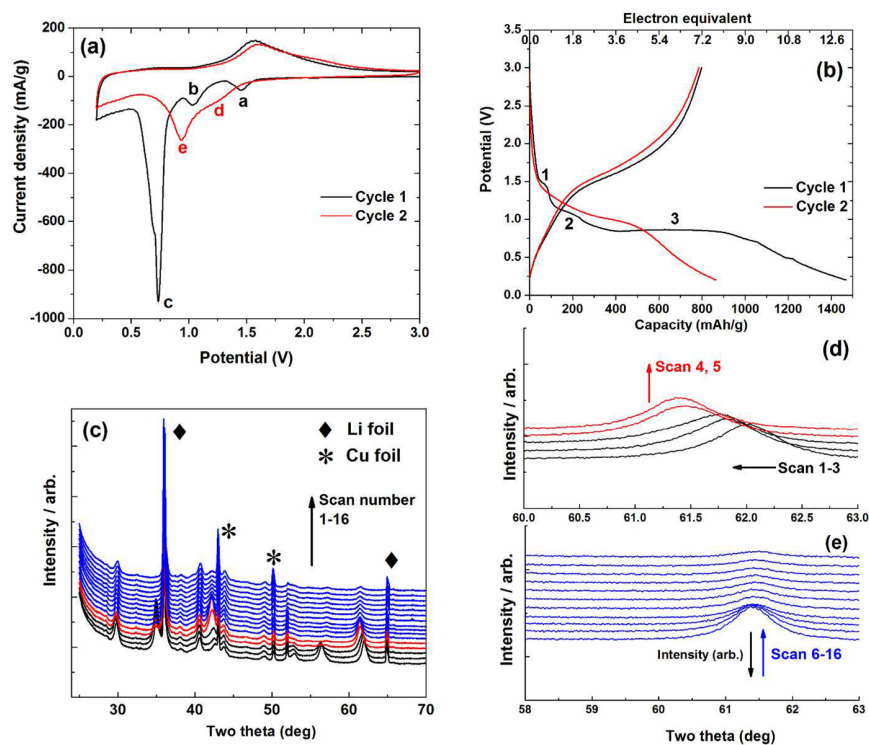


**Figure 4.** (a) Cyclic voltammogram of  $\text{ZnFe}_2\text{O}_4$  electrode at 0.1 mV/s for the first two cycles; (b) galvanostatic profile for cycle 1 and cycle 2 of  $\text{ZnFe}_2\text{O}_4$  electrode at 100 mA/g current density; (c) full two theta range of in situ XRD stack plot during galvanostatic reduction; (d) (044) peak evolution of the first five scans up to 2.0 ee reduction; (e) (044) peak evolution from scan 6 to 16, and scan 16 is the last one during reduction.

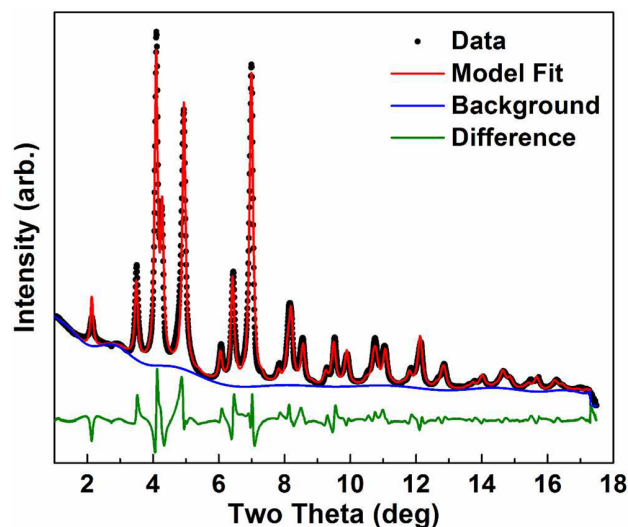


**Figure 5.** Rietveld analysis on 1ee discharged ZFO recovered from cell using ZFO with 10% carbon as the electrode.

Fe Mössbauer spectroscopy where all  $\text{Fe}^{3+}$  ions on the 8a site are reduced at initial uptake of 0.3  $\text{Li}^+$  per formula with migration to 16c site and more  $\text{Fe}^{3+}$  is reduced with further  $\text{Li}^+$  insertion accompanying with both  $\text{Mn}^{2+}$  and  $\text{Fe}^{2+}$  moved to empty 16c sites from 8a sites.<sup>53</sup> A report on  $\text{CoFe}_2\text{O}_4$  spinel material also proposed the cations movement during early lithiation stage and the completion of movement at 2.0 ee depth of discharge indicated by disappearance of spinel diffraction and domination of rock-salt diffraction in the XRD pattern.<sup>54</sup>

With further lithiation, the intensity of the overall spectrum including the peak (044) decreases (Figure 4e), indicating the amorphization of the material. Specifically, the intensity after scan 9 (4 ee discharge at this point) is dramatically (80%) lower than that in scan 6. This phenomenon is also observed in other spinel material even though the amorphization may occur at variable lithiation level, for example, the spinel diffraction disappeared at 2  $\text{Li}^+$  per  $\text{MnFe}_2\text{O}_4$  or  $\text{CoFe}_2\text{O}_4$  formula unit, while insertion of 4  $\text{Li}^+$  per  $\text{MgFe}_2\text{O}_4$  formula unit transformed the crystalline material to an amorphous matrix. To investigate the structure and species evolution further, we pursued ex-situ XANES and EXAFS analysis from partially discharged  $\text{ZnFe}_2\text{O}_4$  electrode.

**X-ray Absorption near Edge Spectroscopy (XANES).** X-ray absorption near edge spectroscopy of both Fe and Zn K-edge for a series of ex-situ electrodes at different level of discharge is measured to track the changes in their oxidation states. Figure 6 shows the XANES of Fe (left) and Zn (right) K-edges of  $\text{ZnFe}_2\text{O}_4$  electrode during various states of the reduction along with the nondischarged electrode. The discharge profiles for all these ex situ electrodes are shown in Figure S4.

In the undischarged state, the Fe K-edge energy (defined as the maximum of the first derivative of  $\chi\mu(E)$ ) is 7126 eV. As reduction begins, the edge shifts slightly to the lower value of 7124 eV at 0.5ee, 2ee, and 4ee. However, a large shift occurs to a metallic-like edge position of 7112 eV is observed once the material has been discharged to 8ee and kept at the same energy when it was reduced to 0.2 V, labeled as “1<sup>st</sup> discharge” in the graph. The spectra at both 8ee and first discharge align well with the Fe metal standard, which is shown in the red dashed lines (left graph).

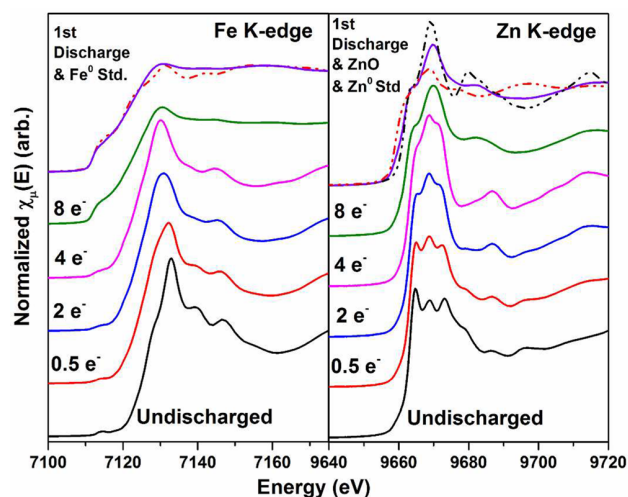


**Figure 6.** XANES spectra of pristine  $\text{ZnFe}_2\text{O}_4$  and different depth of discharge electrodes for Fe (L image) and Zn (R image) edges. The electrodes recovered after the first discharge (top spectra), overlaid with appropriate standards, specifically  $\text{Fe}^0$  (L image, dashed red line),  $\text{ZnO}$  (R image, dashed black line), and  $\text{Zn}^0$  (R image, dashed red line).

The Zn K-edge XANES, however, exhibit less significant shifts in edge energy as the Fe K-edge. In the undischarged state, the edge position is 9664 eV, and the edge energy shifts to slightly lower values of 9663 eV after 4e. When reduced to 0.2 V, the edge is shifted to a final value of 9662 eV, which is still a significantly higher energy than metallic Zn (9659 eV), suggesting a large fraction of the Zn atoms are still in an oxidized state. For comparison, the spectra of Zinc oxide ( $\text{ZnO}$ ) and Zn metal ( $\text{Zn}^0$ ) are also shown with dashed black and dashed red lines, respectively, in which the Zn K-edge XANES spectra of first discharge aligns well with that of  $\text{ZnO}$ , confirming that Zn metal or  $\text{ZnLi}$  alloy has not formed at this discharge state.

**Extended X-ray Absorption Fine Structure Spectroscopy (EXAFS).**  $k^2$ -weighted  $|\chi(R)|$  (Fourier transform of  $\chi(k)$ ) of both the Fe and Zn K-edge spectra are shown in Figure 7. In

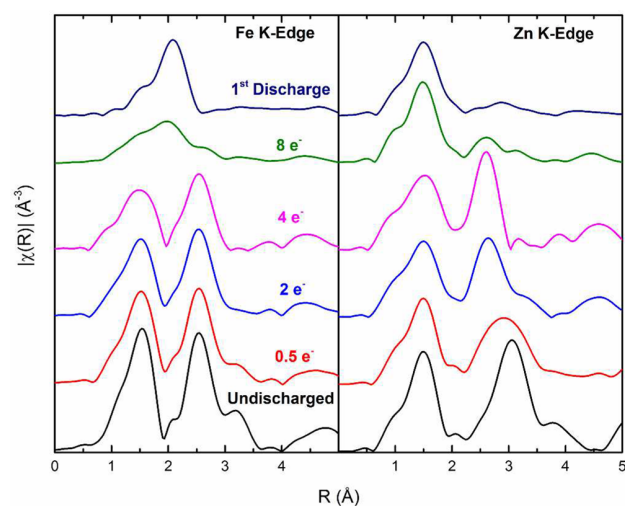


**Figure 7.**  $k^2$ -weighted  $|\chi(R)|$  of both Fe and Zn K-edges at variable depths of discharge: 0.5, 2, 4, 8e, and fully discharged, including the undischarged starting state.

the undischarged state, the Fe K-edge clearly identifies neighboring  $\text{Fe}_{16d}$  and  $\text{Zn}_{8a}$  atoms at distances of 2.6 and 3.2 Å, respectively, consistent with the structure of as synthesized  $\text{ZnFe}_2\text{O}_4$ . Notably, peaks in  $|\chi(R)|$  are about 0.3 Å shorter than the actual interatomic distance due to phase shifts in the scattering process.

At 0.5e reduction, there were no statistically significant changes in Fe K-edge except a reduction in the  $[\text{Fe}]_{16d} - [\text{Zn}]_{8a}$  bond peak at about 3.2 Å. Also, for the Zn K-edge scan, the second shell peak at about 3.1 Å becomes broader at 0.5e. Therefore, there must be a process initiating on  $[\text{Zn}]_{8a}$  at this point. With more lithiation to 2e there are clear changes, including the disappearance of the shoulder peak (ca. 3.2 Å) at Fe edge and the shift to about 2.8 Å of the second shell peak at Zn edge. The bonds on  $[\text{Zn}]_{8a}$  site, about 2.8 Å distance, are significantly shorter than the Zn–Zn distance in common oxides (e.g., Zn–Zn peak is observed at ca. 3.0 Å in  $\text{ZnO}$ ) and significantly longer than that observed for Zn metal (ca. 2.5 Å).<sup>17</sup> Therefore, we infer that  $\text{Zn}^{2+}$  ions should be still in the spinel structure by the time of 2e but start to move from original 8a site from 0.5e.

On the basis of inspection of possible sites in the original  $[\text{Zn}]_{8a}[\text{Fe}_2]_{16d}\text{O}_4$  structure, Zn atoms likely shift to the vacant 16c site, where the expected average  $[\text{Zn}]_{16c} - [\text{Fe}]_{16d}$  distance would be about 2.97 Å. The structure indicating 16c site can be seen in Figure 1. Notably, almost half of the Zn ions migrated to the 16c site in the 1e discharged sample have been determined from the XPD refinement. All the changes in R-space are mirrored in the modeling results. Using both the  $[\text{Zn}]_{8a}[\text{Fe}_2]_{16d}\text{O}_4$  and  $[\text{Zn}]_{16c}[\text{Fe}_2]_{16d}\text{O}_4$  models to fit the Zn K edge at 0.5e data works very well. By the time the electrode has been discharged to 2e, there is no evidence for Zn atoms in the 8a site from the Fe edge spectra due to the disappearance of  $[\text{Fe}]_{16d} - [\text{Zn}]_{8a}$  bond peak at about 3.2 Å and also from the complete shift the second shell peak at Zn K-edge. Fitting both Fe and Zn edge with one  $[\text{Zn}]_{16c}[\text{Fe}_2]_{16d}\text{O}_4$  model confirms this argument, though it is at odds with the DFT results which suggest a 25%/75% split in the old and new sites at two electrons.

Further lithiation to 4e definitely causes Zn to shift from 8a to 16c, as Fe and Zn spectra require both Fe and Zn neighboring atomic contributions to be modeled correctly. The differing backscattering behavior of neighboring Fe and Zn atoms creates a subtle constructive interference behavior for which a single Fe or Zn atom cannot adequately account. By using the  $[\text{Zn}]_{16c}[\text{Fe}_2]_{16d}\text{O}_4$  model, both the Fe and Zn K-edge modeling results are in excellent agreement that the Fe–Zn interatomic distance shifts from  $3.52 \pm 0.02$  Å in the undischarged state with  $[\text{Zn}]_{8a}[\text{Fe}_2]_{16d}\text{O}_4$  structure to  $2.97 \pm 0.02$  Å in  $[\text{Zn}]_{16c}[\text{Fe}_2]_{16d}\text{O}_4$  phase at 4e.

Once reduced to 8e, the original  $\text{ZnFe}_2\text{O}_4$  structure was no longer present, which could be determined from both Fe and Zn K-edges. Fe metal peak at about 2.0 Å is clearly observed in Fe K-edge, and the spectra is fitted very well by using an Fe metal phase. In Zn K-edge, a significant oxygen contribution is present with the first shell peak at about 1.5 Å indicating the presence of  $\text{ZnO}$  phase and the dramatic decrease in the about 2.8 Å peak demonstrates the disappearance of spinel structure. When reduced to 0.2 V, a primarily metallic Fe environment was observed in Fe edge. In Zn edge, the EXAFS modeling and XANES spectra showed the minimal changes from the 8e state except the broadening of the second peak suggests that the Zn is in a highly disordered oxide phase when reduced to 0.2 V. Fe

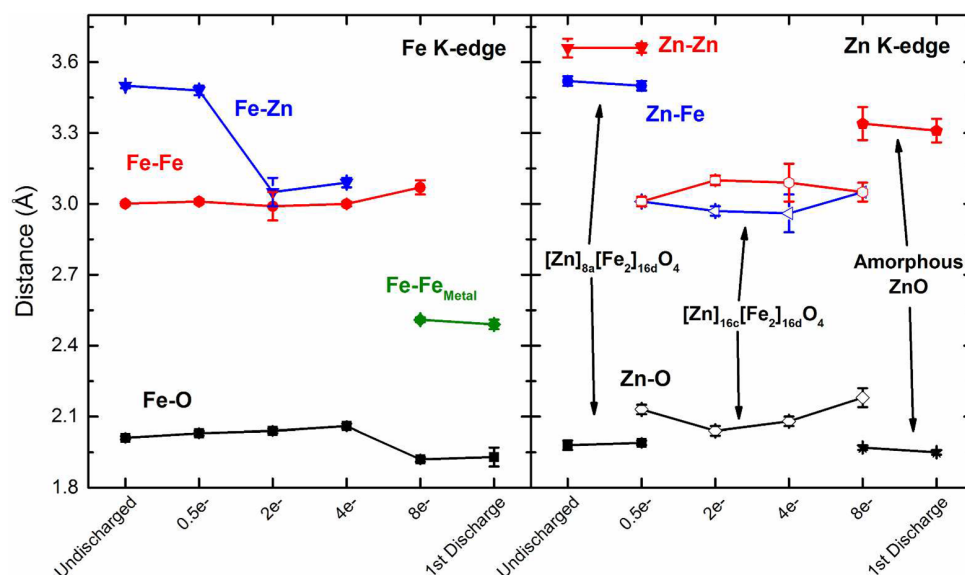


**Figure 8.** Interatomic EXAFS modeling results for both the Fe and Zn K-edge during the initial discharge. The Zn K-edge results directly specify which phase the results are attributed to, either standard  $\text{ZnFe}_2\text{O}_4$  (solid symbols), “shifted”  $\text{ZnFe}_2\text{O}_4$  with Zn atoms moving to vacant sites in the structure (open symbols), and the highly disordered zinc oxide phase (solid symbols).

metal model and amorphous ZnO model fit both Fe and Zn K-edge spectra very well, respectively.

The graphs of the fit for the undischarged, 0.5ee, 2ee, 4ee, 8ee, and reduced to 0.2 V electrodes are shown in Figures S5, S6, and S7, respectively. For nanomaterials, a reduction in the number of neighboring atoms determined through EXAFS analysis may be roughly related to particle size/morphology.<sup>55–57</sup> Number of neighbors for metallic Fe was  $2.8 \pm 0.9$  at 0.2 V discharge voltage. Assuming spherical particle morphology and taking into account the nominal number of neighboring Fe atoms is 8 for bulk bcc Fe metal, this correlates to estimated particle sizes on the order of several nanometers, which is in agreement with amorphous synchrotron XRD of fully discharged electrode (Figure S8).<sup>56</sup> We performed PDF analysis (shown below) of the fully discharged electrode, which confirmed the presence of Fe metal.

The summarized interatomic EXAFS modeling results are shown in Figure 8.  $\text{Zn}^{2+}$  ions begin to migrate at 0.5ee discharge since both phases,  $[\text{Zn}]_{8c}[\text{Fe}_2]_{16d}\text{O}_4$  and  $[\text{Zn}]_{16c}[\text{Fe}_2]_{16d}\text{O}_4$ , are needed to fit EXAFS spectra for Zn K-edge. Absence of EXAFS at 1ee makes it hard to know the species details. However, the XPD of 1ee ex situ electrode that is mentioned above showed that almost half of the  $\text{Zn}^{2+}$  ions migrated to 16c site, which is supportive of and consistent with our EXAFS data.

At 2ee discharge, there was no residual original  $[\text{Zn}]_{8c}[\text{Fe}_2]_{16d}\text{O}_4$  phase, and the EXAFS at Zn K-edge spectra fit well by using one  $[\text{Zn}]_{16c}[\text{Fe}_2]_{16d}\text{O}_4$  new phase. Fe metals and amorphous ZnO are formed at 8ee discharge, which stays the same until reduction to 0.2 V. Previous study on carbon coated ZFO electrode proposed that the initial 0.4ee lithiation did not change the lattice arrangement, while at 0.9ee, all  $\text{Zn}^{2+}$  ions migrated from 8a to 16c site. Their work showed similar phenomena with our EXAFS and XPD results but occurred at different depth of discharge, which was probably due to the faster discharge kinetics by using ZFO electrode with an amorphous carbon layer.<sup>9</sup>

PDF spectra of undischarged and  $\text{ZnFe}_2\text{O}_4$  reduced to 0.2 V with the corresponding fitted structural models are shown in Figure 9. The undischarged  $\text{ZnFe}_2\text{O}_4$  aligned well with the

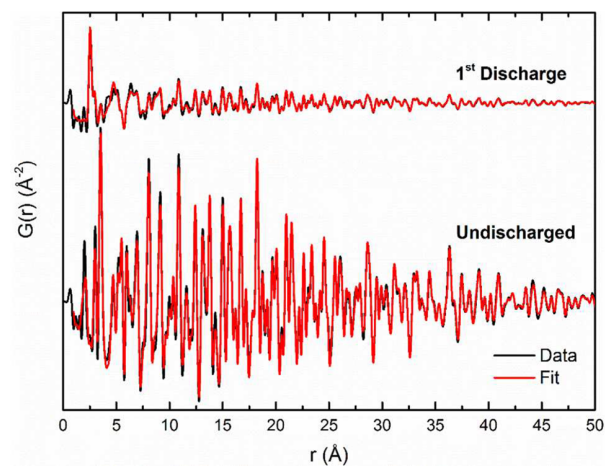


**Figure 9.** PDF spectra of undischarged and fully discharged  $\text{ZnFe}_2\text{O}_4$  pellets (black lines) with corresponding fitted structure results (red lines).

expected crystal structure determined from Rietveld refinement, with an  $R_{\text{wp}}$  value of 17% over the fitted range. The fitted PDF structure results in a crystallite size of  $8.6 \pm 0.4$  nm, which is slightly smaller than the value (11 nm) determined from XRD and TEM.

When reduced to 0.2 V, there is clear emergence of bcc Fe metal in the pattern as evidenced by an intense peak at about 2.5 Å (Figure 9). This was accurately modeled to bcc Fe metal, with corresponding crystallite size of  $1.8 \pm 0.4$  nm. Also observed in the reduced material spectrum is the initial  $\text{ZnFe}_2\text{O}_4$  structure present in a small relative phase percentage to the Fe metal nanoparticles (ca. 6:1 ratio of Fe metal/ $\text{ZnFe}_2\text{O}_4$ ). This suggests that 15% of the active material in the

electrode was not fully reduced even though the cell was discharged at as slow rate as C/200. In addition, there is no unambiguous observation of any zinc oxide species from the PDF analysis. This suggests that this zinc oxide phase is highly disordered and small, which corresponds well to the experimental EXAFS fitting results.

**Comparison of First Reduction and Oxidation XAS at Fe K-edge.** ZnFe<sub>2</sub>O<sub>4</sub> electrodes recovered after first oxidation was also investigated using XAS. The  $k^2$ -weighted  $|\chi(R)|$  spectra are shown in Figure 10. The Fe K-edge of the oxidized

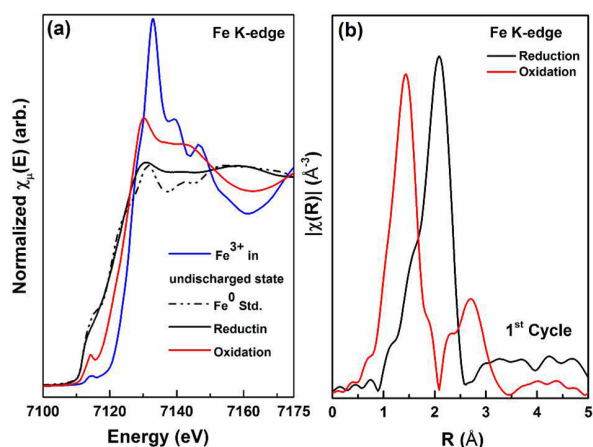


**Figure 10.** Comparison of (a) XANES and (b)  $k^2$ -weighted  $|\chi(R)|$  of Fe K-edge at first discharge (black) and recharge back to 3.0 V (red).

electrode (red line in Figure 10a) is between the edge of reduction and the undischarged electrode, indicating that the oxidized electrode exhibits some reversibility but is cannot be fully oxidized back to 3+. As shown in Figure 10b, it is clear by visual inspection that the local structure around Fe atoms is primarily reversible on the first cycle, with the large metallic-like peak at about 2.2 Å that is observed in the first discharged spectrum is replaced by an oxygen peak at about 1.3 Å and a large, broad peak between 2 and 3 Å when recharged. EXAFS modeling of the cycled spectra confirm the trends observed in Figure 10. When ZnFe<sub>2</sub>O<sub>4</sub> is initially charged, it converts to a highly disordered iron oxide structure, with Fe–O distances of  $1.93 \pm 0.01$  Å and  $3.2 \pm 0.1$  Å along with a Fe–Fe distance of  $3.26 \pm 0.02$  Å. There is no observation of a Fe metal-like distance of about 2.50 Å observed in the first charged state indicating high reversibility of ion species between Fe metal on discharge and FeO on charge at early cycles.

**DFT + U Calculations.** DFT+U calculations were performed to gain further insights into the structural changes in the initial discharge process. To compare with our experimental observations, three key reduction intermediate states, Li<sub>x</sub>ZnFe<sub>2</sub>O<sub>4</sub> ( $x = 0.5, 1, \text{ and } 2$ ), were studied. As shown in Figure 1, in the spinel structure of ZnFe<sub>2</sub>O<sub>4</sub>, Zn<sup>2+</sup> ions occupy the tetrahedral 8a sites and share faces with octahedral 16c vacancy sites, which provide a possible pathway for Zn<sup>2+</sup> ion displacement. The octahedral 16c, tetrahedral 8b and 48f sites are prospective vacancies for Li intercalation. According to our calculations, at 0.5ee of reduction, Li<sup>+</sup> ions all energetically prefer the 16c sites (Figure 11a). In agreement with the XANES measurement, the calculations also observe the spontaneous displacement of the adjacent Zn<sup>2+</sup> ions from the 8a to the 16c site (Figure 11a) upon Li<sup>+</sup> intercalation to the 16c site, which is due to the strong electrostatic repulsion of neighboring octahedral Li<sup>+</sup> and tetrahedral Zn<sup>2+</sup> ions. The amount of displaced Zn<sup>2+</sup> ions to 16c sites at 0.5ee is 25% (Figure 11a), which increases to 50% at 1ee together (Figure 11b) and 75% at 2ee (Figure 11c), while Fe<sup>3+</sup> ions remain at 16d site during this reduction process. Our calculations agree well with in situ XRD, synchrotron refined XPD of 1ee discharged sample, showing that the ratio of Zn<sup>2+</sup> ions in the 16c site with 8a site was close to 1:1 and the occupancy of Fe ions at 16d sites (Table 1 above). Different from the cases at 0.5ee and 1ee, Li<sup>+</sup> ions at 8a sites are observed at 2ee of discharge, as all preferential 16c sites have been filled (Figure 11c). During the discharge process, the cell volume expansion with respect to pristine ZnFe<sub>2</sub>O<sub>4</sub> ( $V_0 = 622.99$  Å<sup>3</sup>),  $\frac{V - V_0}{V_0} \times 100$ , is 2.75% ( $V = 640.15$  Å<sup>3</sup>) at 0.5 ee, where the DFT-optimized bond lengths are consistent with our EXAFS results (Table 2). As discharge progresses, the volume expansion increases to 4.41% ( $V = 650.49$  Å<sup>3</sup>) at 1ee and then rapidly to 22.06% ( $V = 760.40$  Å<sup>3</sup>) upon going to 2ee, a rapid cell expansion, which is accompanied by significant structural distortion (Figure 11c) and likely suggests the tendency for phase separation as observed experimentally. However, the description of the details during such drastic structural dynamics is complex for DFT-based calculations and beyond the scope of the current theoretical study.

We also calculated the average intercalation voltage using the following equation according to the previous study:<sup>58</sup>

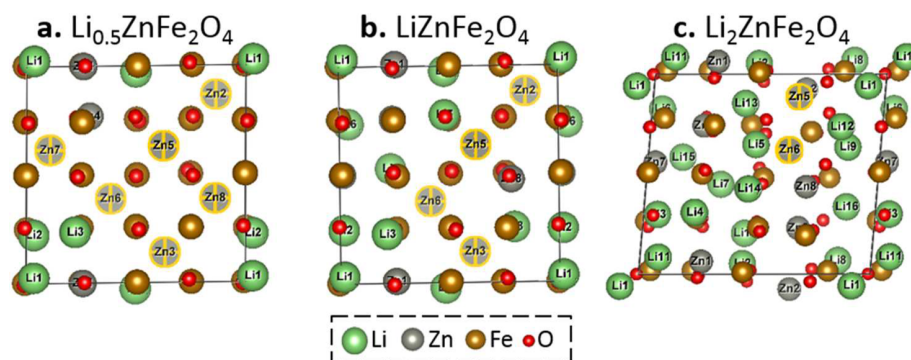


**Figure 11.** Structures of Li<sub>0.5</sub>ZnFe<sub>2</sub>O<sub>4</sub>, LiZnFe<sub>2</sub>O<sub>4</sub>, and Li<sub>2</sub>ZnFe<sub>2</sub>O<sub>4</sub> (gray with yellow circle, Zn<sup>2+</sup> ions in 8a site).

Table 2. DFT Calculated Bond Lengths in  $(\text{Zn})_{8a}\text{Fe}_2\text{O}_4$  and  $\text{Li}_{0.5}(\text{Zn})_{16c, 8a}\text{Fe}_2\text{O}_4$ <sup>a</sup>

	Fe–Fe	Zn–Zn	Fe–Zn	ZnO
ZnFe <sub>2</sub> O <sub>4</sub> from DFT (Å)	3.02	3.70	3.54	2.00
ZnFe <sub>2</sub> O <sub>4</sub> from EXAFS (Å)	3.00 ± 0.02	3.69 ± 0.02	3.52 ± 0.02	1.97 ± 0.02
Li <sub>0.5</sub> ZnFe <sub>2</sub> O <sub>4</sub> from DFT (Å)	3.05	2.98	3.20	2.18
Li <sub>0.5</sub> ZnFe <sub>2</sub> O <sub>4</sub> from EXAFS (Å)	3.02 ± 0.02	±0.02	2.97 ± 0.02	2.15 ± 0.02

<sup>a</sup>For Li<sub>0.5</sub>(Zn)<sub>16c,8a</sub>Fe<sub>2</sub>O<sub>4</sub>, only bonds with Zn<sub>16c</sub> were considered.

$$V = \frac{E(\text{Li}_{x_j}\text{ZnFe}_2\text{O}_4) - E(\text{Li}_{x_i}\text{ZnFe}_2\text{O}_4) - (x_j - x_i)E(\text{Li})}{(x_j - x_i)F}$$

where  $E$  is the DFT calculated total energy for Li<sub>*x*</sub>ZnFe<sub>2</sub>O<sub>4</sub> and bulk metallic lithium (the anode is assumed to be bulk metallic lithium). DFT calculated voltage is 1.64 V at 0.5 ee, 1.58 V at 1 ee, and 0.89 V at 2 ee, respectively, which agree reasonably well with the experimental observations in Figure 4b.

The effect of lithiation on the electronic structure of ZnFe<sub>2</sub>O<sub>4</sub> was also studied. According to the projected density of state (PDOS) (Figure 12), Li atoms at both 16c and 8a sites display an ionic-dominant binding with neighboring O atoms, where Li 2p states remain mostly empty during discharge process. Such phenomenon is different from Li<sub>*x*</sub>SnS<sub>2</sub>, where the covalent nature of Li–S interaction has been reported.<sup>59</sup> The Li 2s and 2p states hybridize more strongly with O 2p states than

O 2s states, and the hybridization with nearby Zn 3d/4s and Fe 3d is also weaker. Thus, the interstitial Li is dominantly stabilized via the ionic interactions with surrounding O atoms. More overlapping in state between O atoms and Li atoms at octahedral 16c sites than with Li atoms at tetrahedral 8a sites is observed (Figure 12), which results in a higher stability of 0.26 eV according to our DFT calculations.

## CONCLUSION

ZnFe<sub>2</sub>O<sub>4</sub> nanoparticles were synthesized by precipitation followed with hydrothermal treatment. The electrochemistry of ZnFe<sub>2</sub>O<sub>4</sub> nanoparticles in lithium-ion batteries showed three plateaus with >1000 mAh/g delivered capacity in the initial discharge and >800 mAh/g (7ee) at first charge. On the basis of the DFT calculations, Li<sup>+</sup> ions were inserted into the 16c site in the lattice without inducing the rearrangement of atoms at the initial reduction of 0.5 electron equivalents. After 0.5ee reduction, Zn<sup>2+</sup> ions migrate from 8a site to the vacant 16c sites based on the fitting results from EXAFS, where synchrotron refined XPD of LiZnFe<sub>2</sub>O<sub>4</sub> reduction sample showed that the ratio of Zn<sup>2+</sup> ions in the 16c site with 8a site was close to 1:1. All these data are consistent with the structure of LiZnFe<sub>2</sub>O<sub>4</sub> from DFT calculations in which 50% Zn<sup>2+</sup> ions are migrated into 16c sites. The DFT calculations also show the structure of Li<sub>2</sub>ZnFe<sub>2</sub>O<sub>4</sub>, in which Li<sup>+</sup> ions at 8a sites are observed as all preferential 16c sites have been filled and where the rapid cell expansion to 23.90% accompanied by significant structural distortion. From EXAFS, Fe metal was formed at 8ee concurrent with an amorphous ZnO phase, which indicates that Fe<sup>3+</sup> was reduced ahead of Zn<sup>2+</sup> ions.

We also found no evidence for the ZnLi alloy even at the reduction limit of 0.2 V, suggesting that six of the electrons delivered on the first discharge can be accounted for by reduction of ZFO. We also demonstrated that the recharged electrode consists of ZnO and FeO, with no evidence for Fe<sub>2</sub>O<sub>3</sub>. Hence, four of the seven electrons measured on recharge can actually be accounted for by the Zn and Fe in the system. Our results suggest that capacity above stoichiometric reactions in ZFO electrodes can be ascribed to carbon and electrolyte electrochemical activity, in which 2ee are attributed to carbon electrochemical activity, while the remaining 5ee are attributed to electrolyte reaction and SEI layer formation.

## ASSOCIATED CONTENT

### Supporting Information

The Supporting Information is available free of charge on the ACS Publications website at DOI: 10.1021/acs.chemmater.7b00467.

First discharge and charge curve of controller cell without ZnFe<sub>2</sub>O<sub>4</sub> active material; voltage profile for fully discharge and 1 ee discharge electrodes used in XPD measurement; Rietveld analysis on ZnFe<sub>2</sub>O<sub>4</sub> as synthesized material from synchrotron source XRD; discharge

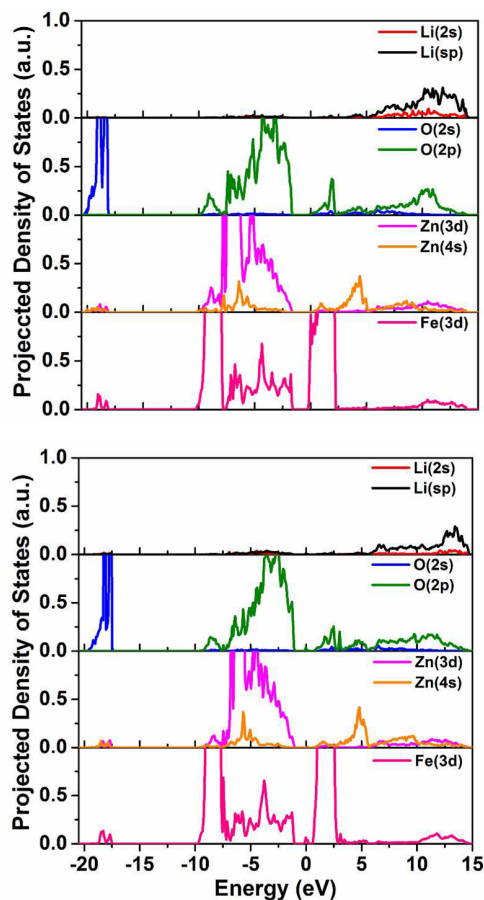


Figure 12. Projected density of states for Li at 16c (top) and 8a (bottom) sites of Li<sub>0.125</sub>ZnFe<sub>2</sub>O<sub>4</sub>.

profiles for electrodes used in ex situ X-ray absorption measurement; EXAFS fit for undischarged, 0.5 ee, 2 ee, 8 ee, and the first discharge electrode; comparison of XPD pattern for undischarged and fully discharged ZnFe<sub>2</sub>O<sub>4</sub> electrode (PDF)

## AUTHOR INFORMATION

### Corresponding Authors

\*E-mail: amy.marschilok@stonybrook.edu.

\*E-mail: kenneth.takeuchi.1@stonybrook.edu.

\*E-mail: esther.takeuchi@stonybrook.edu.

### ORCID

Ping Liu: 0000-0001-8363-070X

Amy C. Marschilok: 0000-0001-9174-0474

Esther S. Takeuchi: 0000-0001-8518-1047

### Notes

The authors declare no competing financial interest.

## ACKNOWLEDGMENTS

The work described in these studies was funded as part of the Center for Mesoscale Transport Properties (m2M), an Energy Frontier Research Center supported by the U.S. Department of Energy, Office of Science, Basic Energy Sciences, under Award No. DE-SC0012673. MRCAT operations are supported by the Department of Energy and the MRCAT member institutions. This research used resources of the Advanced Photon Source, a U.S. Department of Energy (DOE) Office of Science User Facility operated for the DOE Office of Science by Argonne National Laboratory under Contract No. DE-AC02-06CH11357. Use of the National Synchrotron Light Source II, Brookhaven National Laboratory, was supported by the U.S. Department of Energy, Office of Science, Office of Basic Energy Sciences, under Contract No. DE-SC0012704. The authors express their appreciation to Eric Dooryhee, Milinda Abeykoon, Jianming Bai, and Sanjit Ghose for helpful discussions related to X-ray powder diffraction experimental setup and refinement. We thank Chung Chueh-Cheng for assistance with TEM measurements.

## REFERENCES

- (1) NuLi, Y. N.; Chu, Y. Q.; Qin, Q. Z. Nanocrystalline ZnFe<sub>2</sub>O<sub>4</sub> and Ag-Doped ZnFe<sub>2</sub>O<sub>4</sub> Films Used as New Anode Materials for Li-Ion Batteries. *J. Electrochem. Soc.* **2004**, *151*, A1077–A1083.
- (2) Sharma, Y.; Sharma, N.; Rao, G. V. S.; Chowdari, B. V. R. Li-Storage and Cyclability of Urea Combustion Derived ZnFe<sub>2</sub>O<sub>4</sub> as Anode for Li-Ion Batteries. *Electrochim. Acta* **2008**, *53*, 2380–2385.
- (3) Ding, Y.; Yang, Y. F.; Shao, H. X. High Capacity ZnFe<sub>2</sub>O<sub>4</sub> Anode Material for Lithium Ion Batteries. *Electrochim. Acta* **2011**, *56*, 9433–9438.
- (4) Guo, X.; Lu, X.; Fang, X.; Mao, Y.; Wang, Z.; Chen, L.; Xu, X.; Yang, H.; Liu, Y. Lithium Storage in Hollow Spherical ZnFe<sub>2</sub>O<sub>4</sub> as Anode Materials for Lithium Ion Batteries. *Electrochem. Commun.* **2010**, *12*, 847–850.
- (5) Teh, P. F.; Sharma, Y.; Pramana, S. S.; Srinivasan, M. Nanoweb Anodes Composed of One-Dimensional, High Aspect Ratio, Size Tunable Electrospun ZnFe<sub>2</sub>O<sub>4</sub> Nanofibers for Lithium Ion Batteries. *J. Mater. Chem.* **2011**, *21*, 14999–15008.
- (6) Xing, Z.; Ju, Z.; Yang, J.; Xu, H.; Qian, Y. One-Step Hydrothermal Synthesis of ZnFe<sub>2</sub>O<sub>4</sub> Nano-Octahedrons as a High Capacity Anode Material for Li-Ion Batteries. *Nano Res.* **2012**, *5*, 477–485.
- (7) Sui, J.; Zhang, C.; Hong, D.; Li, J.; Cheng, Q.; Li, Z.; Cai, W. Facile Synthesis of MWCNT-ZnFe<sub>2</sub>O<sub>4</sub> Nanocomposites as Anode Materials for Lithium Ion Batteries. *J. Mater. Chem.* **2012**, *22*, 13674–13681.
- (8) Song, W. T.; Xie, J.; Liu, S. Y.; Cao, G. S.; Zhu, T. J.; Zhao, X. B. Self-Assembly of a ZnFe<sub>2</sub>O<sub>4</sub>/Graphene Hybrid and Its Application as a High-Performance Anode Material for Li-Ion Batteries. *New J. Chem.* **2012**, *36*, 2236–2241.
- (9) Bresser, D.; Paillard, E.; Kloepsch, R.; Krueger, S.; Fiedler, M.; Schmitz, R.; Baither, D.; Winter, M.; Passerini, S. Carbon Coated ZnFe<sub>2</sub>O<sub>4</sub> Nanoparticles for Advanced Lithium-Ion Anodes. *Adv. Energy Mater.* **2013**, *3*, 513–523.
- (10) Jiang, B. B.; Han, C. P.; Li, B.; He, Y. J.; Lin, Z. Q. In-Situ Crafting of ZnFe<sub>2</sub>O<sub>4</sub> Nanoparticles Impregnated within Continuous Carbon Network as Advanced Anode Materials. *ACS Nano* **2016**, *10*, 2728–2735.
- (11) Wang, Q. X.; Yue, H. Y.; Du, T.; Zhang, W. L.; Qiao, Y.; Dong, H. Y.; Yin, Y. H.; Yang, S. T. A Particle-Carbon Matrix Architecture for Long-Term Cycle Stability of ZnFe<sub>2</sub>O<sub>4</sub> Anode. *RSC Adv.* **2016**, *6*, 35110–35117.
- (12) Cabo-Fernandez, L.; Mueller, F.; Passerini, S.; Hardwick, L. J. In Situ Raman Spectroscopy of Carbon-Coated ZnFe<sub>2</sub>O<sub>4</sub> Anode Material in Li-Ion Batteries - Investigation of SEI growth. *Chem. Commun.* **2016**, *52*, 3970–3973.
- (13) Rezvani, S. J.; Ciambezi, M.; Gunnella, R.; Minicucci, M.; Munoz, M. A.; Nobili, F.; Pasqualini, M.; Passerini, S.; Schreiner, C.; Trapananti, A.; Witkowska, A.; Di Cicco, A. Local Structure and Stability of SEI in Graphite and ZFO Electrodes Probed by As K-Edge Absorption Spectroscopy. *J. Phys. Chem. C* **2016**, *120*, 4287–4295.
- (14) Chen, C. J.; Greenblatt, M.; Waszczak, J. V. Lithium Insertion Reactions of Spinels: Effect of the distribution and Reducibility of Cations in Selected Manganite and Zinc Spinels. *Mater. Res. Bull.* **1986**, *21*, 609–619.
- (15) Thackeray, M. M.; David, W. I. F.; Goodenough, J. B. Structural Characterization of the Lithiated Iron Oxides Li<sub>1-x</sub>Fe<sub>3</sub>O<sub>4</sub> and Li<sub>x</sub>Fe<sub>2</sub>O<sub>3</sub> (0 < x < 2). *Mater. Res. Bull.* **1982**, *17*, 785–793.
- (16) Tarascon, J. M.; Poizot, P.; Laruelle, S.; Grugeon, S.; Dupont, L. Nano-Sized Transition-Metal Oxides as Negative-Electrode Materials for Lithium-Ion Batteries. *Nature* **2000**, *407*, 496–499.
- (17) Pelliccione, C. J.; Ding, Y.; Timofeeva, E. V.; Segre, C. U. In Situ XAFS Study of the Capacity Fading Mechanisms in ZnO Anodes for Lithium-Ion Batteries. *J. Electrochem. Soc.* **2015**, *162*, A1935–A1939.
- (18) Bresser, D.; Paillard, E.; Kloepsch, R.; Krueger, S.; Fiedler, M.; Schmitz, R.; Baither, D.; Winter, M.; Passerini, S. Carbon Coated ZnFe<sub>2</sub>O<sub>4</sub> Nanoparticles for Advanced Lithium-Ion Anodes. *Adv. Energy Mater.* **2013**, *3*, 513–23.
- (19) Ding, Y.; Yang, Y.; Shao, H. High Capacity ZnFe<sub>2</sub>O<sub>4</sub> Anode Material for Lithium Ion Batteries. *Electrochim. Acta* **2011**, *56*, 9433–9438.
- (20) Yue, H.; Wang, Q.; Shi, Z.; Ma, C.; Ding, Y.; Huo, N.; Zhang, J.; Yang, S. Porous Hierarchical Nitrogen-doped Carbon Coated ZnFe<sub>2</sub>O<sub>4</sub> Composites as High Performance Anode Materials for Lithium Ion Batteries. *Electrochim. Acta* **2015**, *180*, 622–628.
- (21) Kim, J. G.; Kim, Y.; Noh, Y.; Kim, W. B. Formation of Carbon-Coated ZnFe<sub>2</sub>O<sub>4</sub> Nanowires and Their Highly Reversible Lithium Storage Properties. *RSC Adv.* **2014**, *4*, 27714–27721.
- (22) Thankachan, R. M.; Rahman, M. M.; Sultana, I.; Glushenkov, A. M.; Thomas, S.; Kalarikkal, N.; Chen, Y. Enhanced Lithium Storage in ZnFe<sub>2</sub>O<sub>4</sub>-C Nanocomposite Produced by a Low-Energy Ball Milling. *J. Power Sources* **2015**, *282*, 462–470.
- (23) Hameed, A. S.; Bahiraei, H.; Reddy, M. V.; Shoushtari, M. Z.; Vittal, J. J.; Ong, C. K.; Chowdari, B. V. Lithium Storage Properties of Pristine and (Mg, Cu) Codoped ZnFe<sub>2</sub>O<sub>4</sub> Nanoparticles. *ACS Appl. Mater. Interfaces* **2014**, *6*, 10744–10753.
- (24) Cherian, C. T.; Reddy, M. V.; Rao, G. V. S.; Sow, C. H.; Chowdari, B. V. R. Li-Cycling Properties of Nano-Crystalline (Ni<sub>1-x</sub>Zn<sub>x</sub>)Fe<sub>2</sub>O<sub>4</sub> (0 ≤ x ≤ 1). *J. Solid State Electrochem.* **2012**, *16*, 1823–1832.
- (25) Lavela, P.; Tirado, J. L.; Womes, M.; Jumas, J. C. Elucidation of Capacity Fading on CoFe<sub>2</sub>O<sub>4</sub> Conversion Electrodes for Lithium

- Batteries Based on  $^{57}\text{Fe}$  Mössbauer Spectroscopy. *J. Electrochem. Soc.* **2009**, *156*, A589–A594.
- (26) Lavela, P.; Tirado, J. L.  $\text{CoFe}_2\text{O}_4$  and  $\text{NiFe}_2\text{O}_4$  Synthesized by Sol–Gel Procedures for Their Use as Anode Materials for Li Ion Batteries. *J. Power Sources* **2007**, *172*, 379–387.
- (27) Aldon, L.; Jumas, J. C. Lithium-Induced Conversion Reaction in Wüstite  $\text{Fe}_{1-x}\text{O}$  Studied by  $^{57}\text{Fe}$  Mössbauer Spectroscopy. *Solid State Sci.* **2012**, *14*, 354–361.
- (28) Broussard, L. Disproportionation of wüstite. *J. Phys. Chem.* **1969**, *73*, 1848–1854.
- (29) Sano, T.; Tsuji, M.; Tamaura, Y. Effect of Foreign Cation of Zn(II) or Mn(II) Ion in FeO-Wüstite on Its Disproportionation Reaction Below  $575^\circ\text{C}$ . *Solid State Ionics* **1997**, *104*, 311–317.
- (30) Zhang, W.; Bock, D. C.; Pelliccione, C. J.; Li, Y.; Wu, L.; Zhu, Y.; Marschilok, A. C.; Takeuchi, E. S.; Takeuchi, K. J.; Wang, F. Insights into Ionic Transport and Structural Changes in Magnetite during Multiple-Electron Transfer Reactions. *Adv. Energy Mater.* **2016**, *6*, 1502471.
- (31) Ravel, B.; Newville, M. J. Athena, Artemis, Hephaestus: Data Analysis for X-ray Absorption Spectroscopy using IFEFFIT. *J. Synchrotron Radiat.* **2005**, *12*, 537–541.
- (32) López, F. A.; López-Delgado, A.; Martín de Vidales, J. L.; Vila, E. Synthesis of Nanocrystalline Zinc Ferrite Powders from Sulphuric Pickling Waste Water. *J. Alloys Compd.* **1998**, *265*, 291–296.
- (33) Jette, E. R.; Foote, F. An X-Ray Study of the Wuestite ( $\text{Fe O}$ ) Solid Solutions. *J. Chem. Phys.* **1933**, *1*, 29–36.
- (34) Owen, E. A.; Yates, E. L. Precision Measurements of Crystal Parameters. *Philos. Mag.* **1933**, *15*, 472–488.
- (35) Mustre de Leon, J.; Rehr, J. J.; Zabinsky, S. I.; Albers, R. C. Ab initio Curved-Wave X-ray Absorption Fine Structure. *Phys. Rev. B: Condens. Matter Mater. Phys.* **1991**, *44*, 4146–4156.
- (36) Rehr, J. J.; Mustre de Leon, J.; Zabinsky, S. I.; Albers, R. C. Theoretical X-ray Absorption Fine Structure Standards. *J. Am. Chem. Soc.* **1991**, *113*, 5135–5140.
- (37) Hammersley, A. P.; Svensson, S. O.; Hanfland, M.; Fitch, A. N.; Hausermann, D. Two-Dimensional Detector Software: From Real Detector to Idealised Image or Two Theta Scan. *High Pressure Res.* **1996**, *14*, 235–248.
- (38) Toby, B. H.; Von Dreele, R. B. GSAS-II: the Genesis of a Modern Open-Source all Purpose Crystallography Software Package. *J. Appl. Crystallogr.* **2013**, *46*, 544–549.
- (39) Juhas, P.; Davis, T.; Farrow, C. L.; Billinge, S. J. L. PDFgetX3: a Rapid and Highly Automatable Program for Processing Powder Diffraction Data into Total Scattering Pair Distribution Functions. *J. Appl. Crystallogr.* **2013**, *46*, 560–566.
- (40) Farrow, C. L.; Juhas, P.; Liu, J. W.; Bryndin, D.; Bozin, E. S.; Bloch, J.; Proffen, T.; Billinge, S. J. L. PDFfit2 and PDFgui: Computer Programs for Studying Nanostructure in Crystals. *J. Phys.: Condens. Matter* **2007**, *19*, 335219.
- (41) Kresse, G.; Furthmüller, J. Efficiency of Ab-Initio Total Energy Calculations for Metals and Semiconductors Using a Plane-Wave Basis Set. *Comput. Mater. Sci.* **1996**, *6*, 15–50.
- (42) Kresse, G.; Furthmüller, J. Efficient Iterative Schemes for Ab Initio Total-Energy Calculations Using a Plane-Wave Basis Set. *Phys. Rev. B: Condens. Matter Mater. Phys.* **1996**, *54*, 11169–11186.
- (43) Blöchl, P. E. Projector Augmented-Wave Method. *Phys. Rev. B: Condens. Matter Mater. Phys.* **1994**, *50*, 46–72.
- (44) Perdew, J. P.; Burke, K.; Ernzerhof, M. Generalized Gradient Approximation Made Simple. *Phys. Rev. Lett.* **1996**, *77*, 3865–3868.
- (45) Schiessl, W.; Potzel, W.; Karzel, H.; Steiner, M.; Kalvius, G. M.; et al. Magnetic Properties of the  $\text{ZnFe}_2\text{O}_4$  Spinel. *Phys. Rev. B: Condens. Matter Mater. Phys.* **1996**, *53*, 9143–9152.
- (46) Scherrer, P. *Nachrichten von der Gesellschaft der Wissenschaften zu Göttinger* **1918**, 98–100.
- (47) Patterson, A. L. The Scherrer Formula for X-ray Particle Size Determination. *Phys. Rev.* **1939**, *56*, 978–982.
- (48) Zhong, X. B.; Yang, Z. Z.; Wang, H. Y.; Lu, L.; Jin, B.; Zha, M.; Jiang, Q. C. A Novel Approach to Facilely Synthesize Mesoporous  $\text{ZnFe}_2\text{O}_4$  Nanorods for Lithium Ion Batteries. *J. Power Sources* **2016**, *306*, 718–723.
- (49) Qiao, H.; Fei, Y. Q.; Chen, K.; Cui, R. R.; Wei, Q. F. Electrospun Synthesis and Electrochemical Property of Zinc Ferrite Nanofibers. *Ionics* **2016**, *22*, 967–974.
- (50) Zhang, J.; Song, J. M.; Niu, H. L.; Mao, C. J.; Zhang, S. Y.; Shen, Y. H.  $\text{ZnFe}_2\text{O}_4$  Nanoparticles: Synthesis, Characterization, and Enhanced Gas Sensing Property for Acetone. *Sens. Actuators, B* **2015**, *221*, 55–62.
- (51) Di Cicco, A.; Giglia, A.; Gunnella, R.; Koch, S. L.; Mueller, F.; Nobili, F.; Pasqualini, M.; Passerini, S.; Tossici, R.; Witkowska, A. SEI Growth and Depth Profiling on ZFO Electrodes by Soft X-Ray Absorption Spectroscopy. *Adv. Energy Mater.* **2015**, *5*, 1500642.
- (52) Permien, S.; Indris, S.; Schurmann, U.; Kienle, L.; Zander, S.; Doyle, S.; Bensch, W. What Happens Structurally and Electronically during the Li Conversion Reaction of  $\text{CoFe}_2\text{O}_4$  Nanoparticles: An Operando XAS and XRD Investigation. *Chem. Mater.* **2016**, *28*, 434–444.
- (53) Permien, S.; Hain, H.; Scheuermann, M.; Mangold, S.; Mereacre, V.; Powell, A. K.; Indris, S.; Schurmann, U.; Kienle, L.; Duppel, V.; Harm, S.; Bensch, W. Electrochemical Insertion of Li into nanocrystalline  $\text{MnFe}_2\text{O}_4$ : a study of the reaction mechanism. *RSC Adv.* **2013**, *3*, 23001–23014.
- (54) Permien, S.; Indris, S.; Schurmann, U.; Kienle, L.; Zander, S.; Doyle, S.; Bensch, W. What Happens Structurally and Electronically during the Li Conversion Reaction of  $\text{CoFe}_2\text{O}_4$  Nanoparticles: An Operando XAS and XRD Investigation. *Chem. Mater.* **2016**, *28*, 434–444.
- (55) Calvin, S.; Luo, S. X.; Caragianis-Broadbridge, C.; McGuinness, J. K.; Anderson, E.; Lehman, A.; Wee, K. H.; Morrison, S. A.; Kurihara, L. K. Comparison of Extended X-Ray Absorption Fine Structure and Scherrer Analysis of X-Ray Diffraction as Methods for Determining Mean Sizes of Polydisperse Nanoparticles. *Appl. Phys. Lett.* **2005**, *87*, 233102.
- (56) Calvin, S.; Miller, M. M.; Goswami, R.; Cheng, S.-F.; Mulvaney, S. P.; Whitman, L. J.; Harris, V. G. Determination of Crystallite Size in a Magnetic Nanocomposite Using Extended X-Ray Absorption Fine Structure. *J. Appl. Phys.* **2003**, *94*, 778–783.
- (57) Frenkel, A. I.; Hills, C. W.; Nuzzo, R. G. A View from the Inside: Complexity in the Atomic Scale Ordering of Supported Metal Nanoparticles. *J. Phys. Chem. B* **2001**, *105*, 12689–12703.
- (58) Aydinol, M. K.; Kohan, A. F.; Ceder, G.; Cho, K.; Joannopoulos, J. Ab initio study of lithium intercalation in metal oxides and metal dichalcogenides. *Phys. Rev. B: Condens. Matter Mater. Phys.* **1997**, *56*, 1354–1365.
- (59) Liu, Z.; Deng, H.; Mukherjee, P. P. Evaluating Pristine and Modified  $\text{SnS}_2$  as a Lithium-Ion Battery Anode: A First-Principles Study. *ACS Appl. Mater. Interfaces* **2015**, *7*, 4000–4009.